Electrochemical characterization of localized corrosion mechanism of ALD Al2O3-coated copper for microelectronic application

Romain Haeffele, Sabrina Marcelin, Lucile Broussous, Lucie Mazet, Bernard Normand

Corrosion Science 234 (2024) 112135

Contents lists available at ScienceDirect

Corrosion Science

journal homepage: www.elsevier.com/locate/corsci

Electrochemical characterization of localized corrosion mechanism of ALD Al_2O_3-coated copper for microelectronic application

Romain Haeffele [a,b], Sabrina Marcelin [b,*], Lucile Broussous [a], Lucie Mazet [a], Bernard Normand [b]

[a] STMicroelectronics, 850 rue Jean Monnet, Crolles 38920, France
[b] INSA Lyon, CNRS, UCBL1, MATEIS UMR 5510, Villeurbanne 69621, France

ARTICLE INFO

Keywords:
(A) Copper
(A) Electronic materials
(B) EIS
(B) SECM
(C) oxide coatings

ABSTRACT

To achieve performance and reliability in microelectronics devices, copper interconnections must be protected from aggressive environment during the manufacturing process and throughout the life of the devices. Atomic Layer Deposition Al_2O_3 thin films has been used as a compatible layer with key integration process steps, as well as being corrosion-resistant in neutral media. However, electrochemical tests in aggressive environment have revealed that the alumina prematurely failed to protect copper from localized corrosion. In this study, local and global electrochemical techniques have been employed to evaluate the reactivity of copper at multiple scales and to elucidate the underlying corrosion mechanisms.

1. Introduction

Currently, the most used materials for chips to package connections in microelectronics devices are aluminum (Al) pads and copper (Cu) wires. However, the wire-bonding process used to connect these components can lead to the formation of inter-metallic compounds, which can cause galvanic corrosion [1–3], as well as the creation of Kirkendall voids [4,5]. These issues significantly limit the long-term reliability of the microelectronic packaging. To address concerns regarding cost-effectiveness, performance, and reliability of materials in the semiconductor industry. Copper wirebonding on copper pad (Cu-to-Cu bonding) approach was periodically evaluated since the early 2000 s, but never growth as an industrial application. Challenges and limitations were summarized in 2018 review [6]. Copper is a promising material for microelectronics due to its electrical conductivity ratio of 5:3 to that of aluminum and its high melting point, which greatly reduces the electromigration [7]. The intrinsic properties of electrodeposited copper, such as impurities and microstructure evolution associated with the type of germination/growth, can make it sensitive to corrosion. While copper's oxide film provides some protection against corrosion, it is not as stable, dense, or uniform as passive films formed on other metals like stainless steel [8,9].

The integration of copper bond pad presents a significant challenge for semi-conductor industry. Achieving a controlled surface state of copper is essential to enable reliable connection to the package. Although the manufacturing steps of electronic compounds are performed in very controlled environments, there are many sources of contamination that can lead to corrosion of copper pads during the assembly steps. Furthermore, major concern of copper oxidation takes place at back-end level with difficulties to wire-bond and to perform electrical tests on oxidized surfaces, as copper oxide layer leads to a morphology change of the copper surface [10,11]. Therefore, it is crucial to find an integrable solution to protect copper interconnections from corrosion. This solution must be compatible with key back-end process steps such as electrical probing, wire-bonding, and molding.

Previous studies investigating the corrosion protection of copper pads and their bondability improvement have identified three distinct types of protective coatings [6,12]: (*i*) metallic coatings such as nickel, gold, palladium and less noble metals with their native oxides (*e.g.* Ti), (*ii*) organic coatings such as self-assembled monolayer and (*iii*) Inorganic coatings such as silicon or aluminum oxides. One limitation being to achieve very thin films deposition, it is to note that Al_2O_3 is less mentioned in the literature.

The use of electroless over-pad metallization with a bilayers structure consisting of Ni/Pd [13], Ni/Au [14] or Ni/Au/Pd [14] has been explored. Gold and palladium offer anti-corrosion properties and strong reduction of Kirkendall effect. On the other hand, nickel exhibits remarkable interdiffusion properties regarding copper. But this solution is not desirable due to its high cost and the need for heavy chemical processes and equipment. The literature has also explored the deposition

* Corresponding author.
E-mail address: sabrina.marcelin@insa-lyon.fr (S. Marcelin).

https://doi.org/10.1016/j.corsci.2024.112135
Received 1 February 2024; Received in revised form 9 May 2024; Accepted 12 May 2024
Available online 13 May 2024

of metallic thin films to create an oxide protective layer, such as Ti [15]. Aoh *et al.* deposited thin films of 3.5 nm using magnetron sputtering. They demonstrated that a pure TiO_2 film was formed on the copper pads during back-end steps (sawing and die-mounting) and allowed reliable gold wire bonding. The main issue is the copper migration through the metal coatings and the increase in contact resistivity after bonding. Some researchers have also investigated the use of organic coatings [16, 17]. In their work, Ho *et al.* have demonstrated the feasibility to bond copper wire to copper pad using Self Assembled Monolayer over the copper pad [18]. But the implementation of organic layer is associated with an increase in electrical resistivity at the Cu-Cu interface and the preparation of such layers required sophisticated process. The present study has specifically investigated inorganic coatings, which have received less attention in the literature for the purpose of protecting copper pads. To perform an efficient Cu ball to Cu pad wire-bonding, the inorganic protective film should be as thin as possible while being stable and uniform. Atomic Layer Deposition (ALD) is now a widely used technique in microelectronics production [19]. ALD's ability to deposit nanometer-scale thickness films at relatively low temperature ($< 200°C$) is advantageous as it avoids reaching the temperature limits of integrated component such as microelectronics active materials [20]. Moreover, the ALD layers are reported to contain low defects density which promotes their barrier properties to protect the metal underneath against corrosion [21]. Alumina (Al_2O_3) was chosen as a good starting material for studying protection of copper bond pad due to its good stability in various media [22], strong adhesion to copper [11], and favorable mechanical properties [23].

Many studies have shown that nanoscale ALD oxide layers can enhance the corrosion protection of bulk copper. Daubert *et al.* have shown improved corrosion resistance of copper using ALD-deposited Al_2O_3 and other oxide layers by using electrochemical impedance spectroscopy [24]. However, they also found, that increasing the thickness of the alumina layers beyond 50 nm did not improve the protection. Chai *et al.* conducted a study in the same media with a similar material and process condition [25] and found a stabilization of the corrosion protection above ~20 nm. Among the notable differences between the samples, the copper preparation and its surface state can be mentioned. However, some other parameters may be responsible for the variability observed, thus fully justifying the reproduction of the study for the microelectronic sample. The long-term corrosion protection of ALD Al_2O_3 on copper has already been demonstrated by several authors in neutral sodium chloride solutions. Electrochemical impedance measurements at the corrosion potential were used to evaluate the stability of the 50 nm ALD Al_2O_3 films in neutral 0.1 M NaCl solution over 75 hours [24]. Some studies suggested that the copper corrosion mechanism is caused by alumina dissolving when the pH drop due to O_2 reduction [26–28]. Mirhashemihaghighi *et al.* have also demonstrated that corrosion rates were restricted by dissolved oxygen reduction resulting from mass transport, when exposed to the same media [28]. While ALD alumina demonstrates sealing properties and can provide sufficient initial corrosion protection with films under 50 nm thickness, its enduring stability on low-scaled copper films remains uncertain and requires further investigation.

This study focuses on investigating the corrosion protection properties of an alumina coating applied on a thin copper layer. The use of versatile electrochemical techniques, such as electrochemical impedance spectroscopy, helps to characterise the dielectric layer as well as to investigate the complete degradation mechanisms of the copper bond pads. Aggressive electrochemical tests involving immersion in saline solutions coupled with advanced microscopic observations have been performed to characterize the evolution of the system. This study aims to improve the reliability of copper bond pads by analyzing the local corrosion mechanisms of copper film coated with alumina to predict failures. In other words, the objective is to investigate early stages degradation mechanisms of the system to propose ways of optimizations based on the metallic substrate and the coating material engineering.

2. Experimental part

2.1. Material and surface preparation

Two types of multi-material stacks were used. The first, called "patterned wafer" (Fig. 1.a) reproduced the different nature of layers used in real microelectronic devices with copper pad of 60 μm wide. In order to further study the corrosion mechanism, full-sheet wafer reproducing the stack with lager copper surface area were used (Fig. 1. b). This second kind of material was developed without any pattern and constitute fast process and efficient tool. For the both samples, the base of the wafer is composed of p-type (001) silicon substrate covered with a layer of silicon oxide of 1000 μm, added to get closer to the mechanical behavior of an electronic chip. A bilayer of tantalum and tantalum nitride was physically deposited on the silicon oxide to promote the adhesion of the copper seed layer prior to the final electrodeposition of 3 μm thick copper film. *In-situ* 120 s annealing at 250°C was then performed to stabilize the metal. The surface was then polished to reach a final thickness of 3 μm. The copper surface was then exposed to chemical desoxidation treatment (HF 0.2% for 20 s) prior to coating deposition with a controlled waiting time of 1 hour maximum. The procedure for ALD Al_2O_3 deposition on copper wafer is directly adapted from industrial process at STMicroelectronics. Coatings with nominal thicknesses of 10 nm were deposited using commercial ASM XP8 reactor at a temperature of 150°C. The precursors employed were trimethylaluminium (TMA, $Al(CH_3)_3$) and H_2O (water vapor). One complete ALD cycle is composed of 1.5 s oxidant pulse, 5 s N_2 purge, 225 ms TMA pulse and 2 s N_2 purge, leading to 1.1 Å/cycle growth rate.

2.2. Surface analysis

Surface analyses were performed on patterned wafers, which were carefully assessed for correspondence with the non-patterned wafers. The thin ALD film was examined using scanning transmission electron microscopy (STEM) with an EDS detector to improve film detection and ensure adequate resolution.to compare them with non-patterned wafers.

The observation of the surface state before and after the immersion in aqueous electrolyte was performed using a scanning electron microscope Zeiss Supra 55 with an accelerated voltage of 5 keV and a working distance of 8.5 cm to ensure sufficient surface resolution. Focus Ion Beam (FIB) was used to cut into the local defects using a Tescan Amber G4 instrument using conventional Ga ions source.

X-ray reflectivity (XRR) is a non-destructive technique to measure film thickness below 1 μm [29]. A 17-point mapping was performed on each wafer to control film homogeneity and ensure an accurate ALD layer thickness measurement.

2.3. Electrochemical measurements

Local and global electrochemical measurements were performed on patterned wafer and non-patterned wafer, respectively.

Scanning Electrochemical Microscopy was used to map the local reactivity that occurred on patterned wafer (Fig. 1.a). The selected working mode was the feedback mode, using ferrocenemethanol as the electrochemical mediator. A solution composed of 5 mM NaCl and 2 mM ferrocenemethanol was selected as supporting electrolyte. All SECM measurements were carried out in a faraday cage, using a VERSASTAT low-current modulus. The test-cell was composed of a platinum microelectrode of 10 μm radius as the working electrode, a platinum wire as a counter electrode, and a Ag/AgCl electrode as the reference electrode with a potential of +0.222 V vs SHE. A potential bias of + 0.7 V was applied to the tip to ensure a limiting-current state for the oxidation of Fe^{2+} from the mediator. The SECM scans were performed on an area of 300×300 μm^2 with a step of 5 μm and a measuring speed of 10 μm/s. The complete scan was recorded in 3 hours.

Concerning large-scale measurements, a 3-electrodes cell was

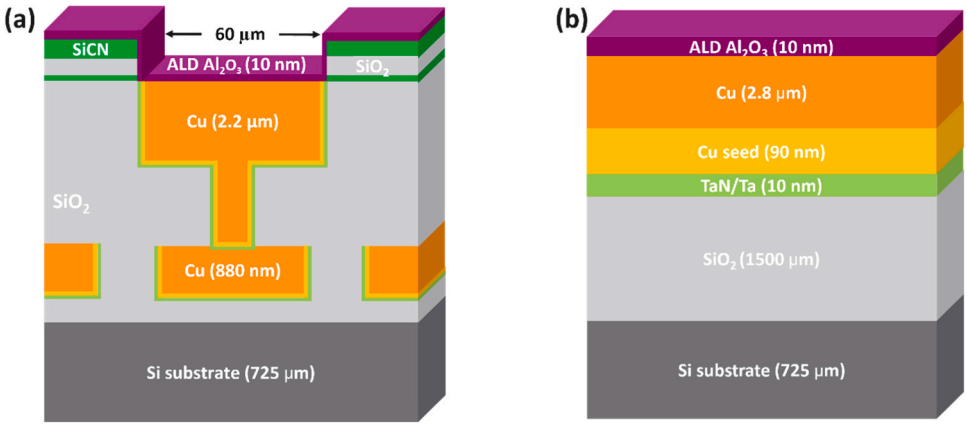

Fig. 1. Schematic representation of multi-layer stack of microelectronic device: (a) patterned wafer and (b) full-sheet wafer.

introduced in a Faraday cage. The working electrode used was the non-patterned Al_2O_3 coated copper (Fig. 1.b), with a constant area of 10 cm^2. This area was chosen to account for the heterogeneous local thickness of the coating and to provide an average electrochemical response. A saturated calomel electrode (SCE) with a potential of +0.241 V *vs* SHE was utilized as the reference electrode, regardless of the electrolytic solution. Distance between reference and working electrode has been fixed to 2 cm. A porous graphite rod was used as the counter electrode. Electrochemical measurements were performed at room temperature using a Gamry Reference 600 potentiostat. Neutral and aerated 0.1 M Na_2SO_4 and 0.1 M NaCl aqueous solutions were used as electrolytes. The first solution was selected as a non-aggressive electrolyte and the second to reproduce the corrosion mode observed during preliminary assembly test. Before performing electrochemical measurements, the samples were cleaned with deionised water and dried under air flow.

Successive electrochemical impedance spectroscopy (EIS) measurements were performed every two hours over a 16 hours period. Impedance measurements were carried out at corrosion potential (E_{corr}) with a voltage amplitude of $\pm$ *10 mV*, in the frequency range from 10 kHz to 2 mHz and with 10 points per decade. Before each EIS measurement, the polarization resistance (R_p) was measured in order to verify the stability of the electrochemical system. The polarization resistance was determined from the slope of the polarization curves obtained at a sweep voltage of 0.5 mV/s close to the corrosion potential ($\pm$ *5 mV* around E_{corr}).

Additional EIS measurements were performed around corrosion potential in either the anodic or cathodic domains ($\pm$ *50 mV vs.* E_{corr}) after 2 hours of immersion at E_{corr}. Prior to acquiring impedance diagrams, the working electrode was polarized at the desired potential for 20 min.

The validity of the results obtained from EIS measurements was defined by Kramers-Kronig transformation ensuring measurement accuracy by identifying the frequency range in which the conditions of linearity, causality, and stationarity are satisfied. The impedance diagrams were fitted using a Python-based free software developed by Orazem and Watson [30] permitting to obtained standard deviation on fitted parameters. The input parameters in the model were first obtained from a graphical analysis of the experimental data [31,32]. To ensure reproducibility of the results, all electrochemical measurements were repeated at least three times.

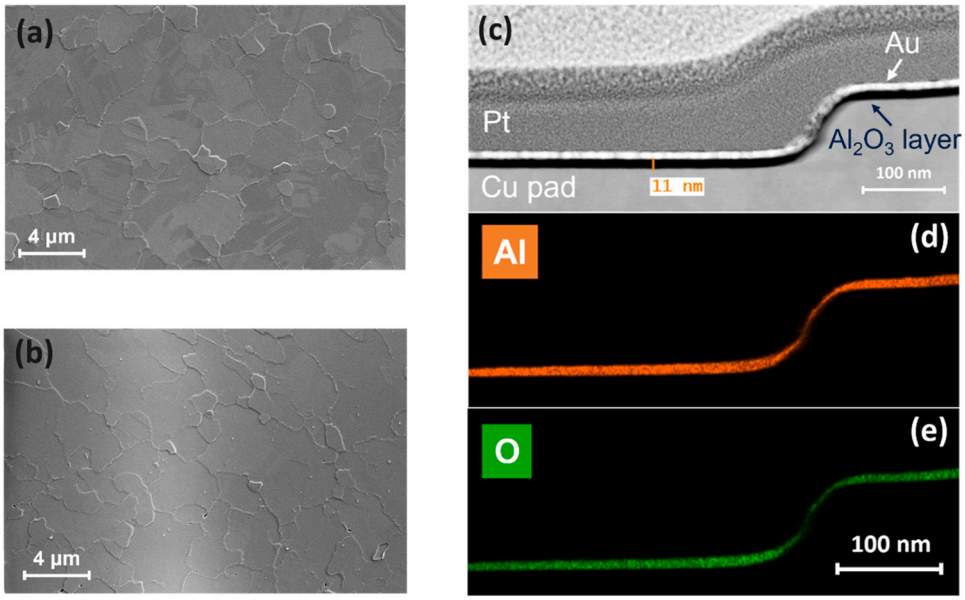

Fig. 2. SEM micrographs of: (a) bare copper substrate and (b) 10 nm-thick Al_2O_3 coated copper as-deposited. Cross sections of alumina coated copper: (c) STEM micrograph and EDS analyses of (d) aluminum and (e) oxygen. Pt & Au layer were deposited for TEM Lamella preparation.

3. Results and discussion

3.1. Surface characterization of Al_2O_3/Cu system

SEM observation before the immersion tests have been performed on bare copper (Fig. 2.a) and copper coated with alumina layer (Fig. 2.b). Crystallographic contrast can be seen with SE detector on the bare Cu sample, evidencing high quality of the surface state. For both samples (with and without ALD layer), small copper hillock surrounded by bigger grains can be observed. Copper grain hillocks defects, a common phenomenon in microelectronics [33,34], arise from variations in normal stress along the grain boundaries, which are influenced by factors such as grain orientation, dimensions, and environment [35]. As shown in Fig. 2.c-e, the ALD Al_2O_3 layer is covering the whole copper surface. The thickness layer was measured to be 11 ± 0.5 *nm*. However, a localized thinning of the layer down to a few nanometers at the stepping edge of the hillocks is observed.

3.2. Electrochemical characterization of the coated copper

3.2.1. Dielectric properties of ALD alumina layer

Fig. 3.a shows an impedance diagram in Bode coordinates, obtained after 1 hour of immersion in the neutral and aerated Na_2SO_4 solution. The ohmic drop contributes to the electrochemical response observed in the high frequencies range, masking the capacitive response of the interface [36]. Thus, to remove this contribution and to enhance the high frequency signal, the diagram was corrected by the value of the electrolyte resistance R_e (152 $\Omega.cm^2$) determined in high frequency range in Nyquist plot, following a procedure described by Orazem *et al.* [36]. The adjusted Bode plot is characterized by a pure capacitive behavior defined by a constant phase angle equal to $-90°$ in high frequency range. It can be assumed that the impedance is only governed by the capacitance of the dielectric film, the double-layer capacitance being neglected [37]. Thus, this electrochemical response is attributed to the 10 nm-thick Al_2O_3 layer. A complex representation of the capacitance (also called Cole-Cole plot [38,39]) shows the evolution of the imaginary capacitance as a function of the real capacitance (Fig. 3.b). The complex capacitance C(ω) is expressed in Eq. 1 as a function of the impedance Z(ω):

$$C(\omega) = \frac{1}{j\omega(Z(\omega) - R_e)} \quad (1)$$

The estimated capacitance of the alumina film C_∞, graphically determined in high frequency range by extrapolation is equal to 6.55×10^{-7} $F.cm^{-2}$. Knowing the thickness of the alumina film δ, the remaining unknown value ε can be determined using the Eq. 2:

$$\varepsilon = \frac{\delta C_\infty}{\varepsilon_0} \quad (2)$$

The dielectric constant was found to be 8, which agrees with data from the literature usually between 8 and 9 for Al_2O_3 thin films [40].

To determine the dielectric properties of the film, an electrical equivalent circuit (EEC) composed of a pure capacitance $C_{Alumina}$ in parallel with a film resistance $R_{Alumina}$ was proposed to fit the experimental data (Fig. 4). The impedance data were corrected by the electrolyte resistance, and therefore this parameter was not included in the model. Fig. 3.a shows a good agreement between experimental and fitted data characterized by a narrow confidence interval (χ^2 value limited to 1.85×10^{-2}). Assuming a constant permittivity along the alumina layer thickness, the resistivity ρ can be obtained using the Eq. 3:

$$\rho = \frac{R}{\delta} \quad (3)$$

All parameters determined from XRR, ellipsometry and EIS measurements are reported in Table 1.

The thickness of the ALD layer determined by XRR and ellipsometry are in agreement. The obtained thickness value, along with the parameters obtained from EIS measurements, enable the assessment of the dielectric parameter of the layer. The alumina resistivity is lower than a value reported in the literature for ALD alumina grown on silicon substrate, which is around 10^{15} Ω.cm for 12 nm-thick alumina [41]. This difference, can be attributed to the heterogeneous thickness of the alumina layer due to the presence of copper hillock, as shown in Fig. 2c-e. The deep understanding of the copper/alumina layer/Na_2SO_4 electrolyte system was necessary prior to investigating the corrosion mechanism in chloride-containing aqueous solution.

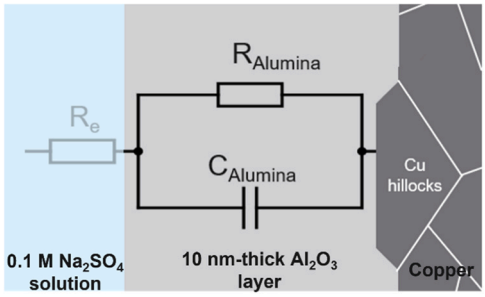

Fig. 4. Electrical equivalent circuit used to fit impedance data obtained for Copper/Alumina layer/Aerated sodium sulfate solution interface.

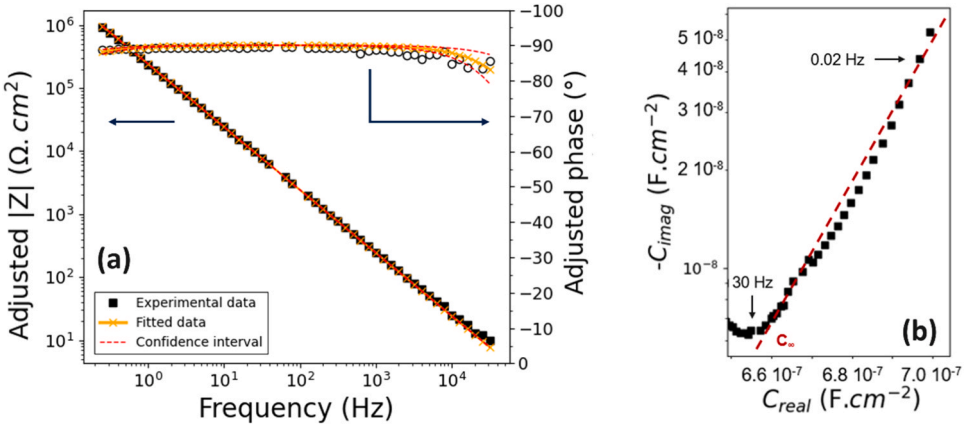

Fig. 3. Electrochemical impedance diagrams obtained for full-sheet wafer after 1 hour of immersion in aerated 0.1 M Na_2SO_4 electrolyte: (a) corrected by ohmic drop in Bode coordinates and (b) in complex capacitance representation.

Table 1
Dielectric parameters obtained for the Al_2O_3 layer deposited on copper from different characterization technics.

δ (XRR) / nm	**δ** (ellipsometry) / nm	**Capacitance** (graphical determination, Fig. 3.b) / F.cm^{-2}	**Capacitance** (obtained from fitting) / F.cm^{-2}	**ε** (calculated from Eq. 2)	**R** (obtained from fitting) / Ω.cm^2	**$\rho_{Alumina}$** (calculated from Eq. 3) / Ω.cm
10.9 *± 0.23*	10.9 *± 2.55*	6.55×10^{-7}	6.56×10^{-7} *± 1.5×10^{-9}*	8	2.97×10^7 *± 7.49×10^6*	2.7×10^{13}

3.2.2. Electrochemical behavior of Cu/Al_2O_3/NaCl interface

The advantage of SECM is to study surface reactivity variations caused by local heterogeneities. Thus, it is particularly dedicated to measure the surface reactivity of electronic microships. Fig. 5.a shows the scanned area delimited by the white square of a copper chip covered by 10 nm-thick Al_2O_3 layer. Around 15 copper pads were scanned over the 300×300 μm^2 surface area. The SECM maps acquired after 4 hours, 24 hours and 32 hours in immersion in a dilute NaCl solution (5 mM) are presented in Fig. 5.b-d, respectively. The current normalized to the bulk limiting current is measured on selected surface. After 4 hours, some localized areas already display higher reactivity, although the recorded current remains below the bulk current. After 24 hours, positive feedback emerges on some copper pads, indicating the triggering of corrosion processes. After 32 hours, current continues to increase over the entire scanned area. This evolution is correlated with the formation of non-protective corrosion products and the thinning and/or dissolution of the Al_2O_3 oxide layer. Based on this observation, global electrochemical measurements were performed on non-patterned full-sheet wafer to investigate the corrosion mechanisms involved.

Impedance measurements were performed on the non-patterned full-sheet wafers after 2 hours of immersion in more concentrated NaCl solution (0.1 M). At E_{corr}, both cathodic and anodic electrochemical processes take place simultaneously. To enhance the contribution of each process, electrochemical impedance spectroscopy was performed under polarisation in both domains (Fig. 6). The shape of the impedance diagrams is modified with the anodic polarisation with a decrease of the maximum phase angle at high frequency and a decrease in low frequency impedance modulus (Fig. 6.a). On the other hand, the cathodic polarisation did not show any high frequency response modification, but the low frequency impedance modulus increases with the over potential (Fig. 6.b). These observations revealed that the electrochemical behavior of Al_2O_3/Cu system in 0.1 M NaCl at E_{corr} is mainly driven by the anodic process.

Fig. 7 shows the adjusted impedance diagrams obtained for the coated copper during time in 0.1 M NaCl electrolyte at corrosion potential. It should be mentioned that the low frequency part of the impedance diagrams was limited to 1 Hz. Values below this frequency exhibited KK error >5% and were therefore excluded from the interpretation of the impedance diagram. However, additional experiments conducted in a deaerated 0.1 M NaCl solution suggest that the low-frequency signature observed may be attributed to limited reactive species such as dissolved oxygen. The diffusion impedance for a semi-infinite film is modelled using a Warburg element [42], and has been previously reported for a copper sheet covered by alumina in aerated solutions [26,28,43]. Direct comparison with other works cannot be done due to the significant differences of sample preparation, resulting in different morphology, chemistry, etc. However, it is assumed that the mechanism of corrosion of copper is rather similar in electrolyte containing chloride and oxygen.

The impedance modulus at 1 Hz is decreasing during time, from

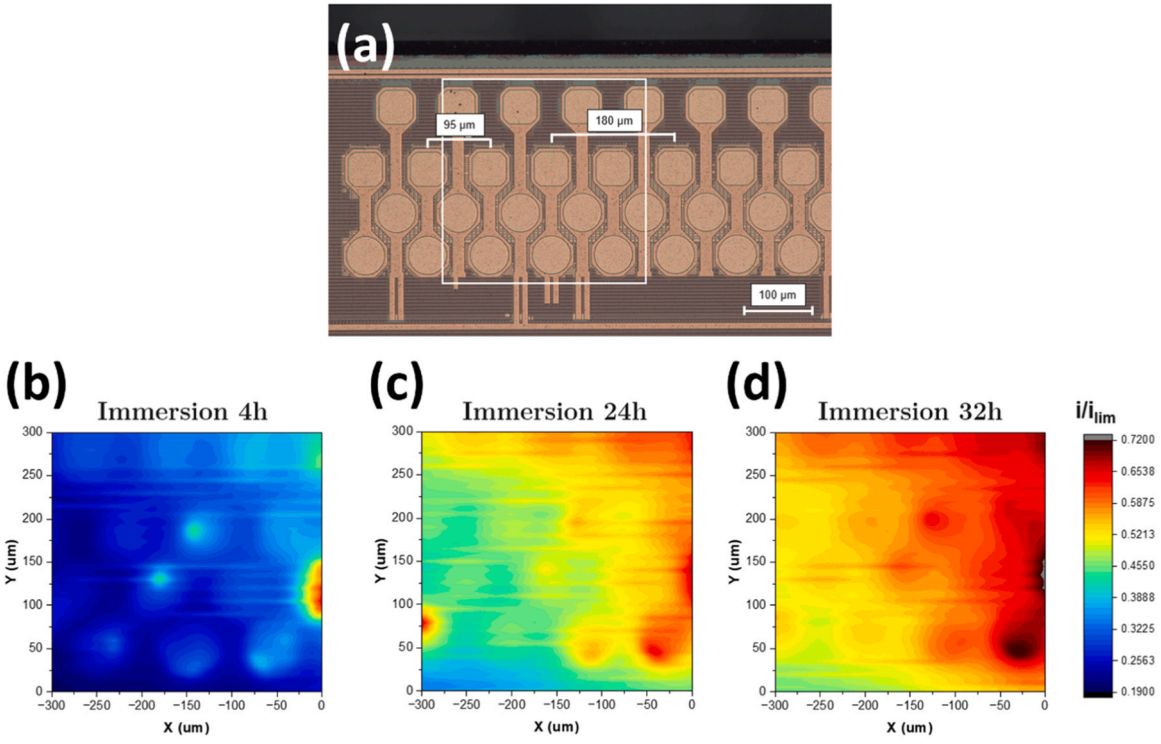

Fig. 5. (a) Optical micrograph of copper pads covered with 10 nm-thick alumina layer. SECM current maps obtained over time after (b) 4 hours, (c) 24 hours and (d) 32 hours of immersion in 5 mM NaCl solution containing 2 mM ferrocenemethanol.

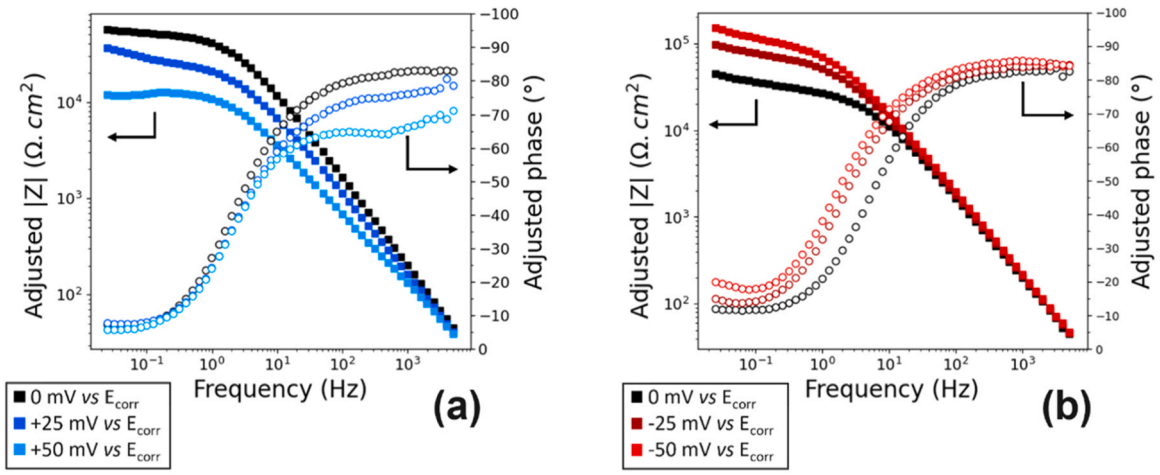

Fig. 6. Adjusted Bode impedance diagrams obtained after 2 hours of immersion in 0.1 M NaCl electrolyte at corrosion potential and around corrosion potential in (a) anodic and (b) cathodic domain.

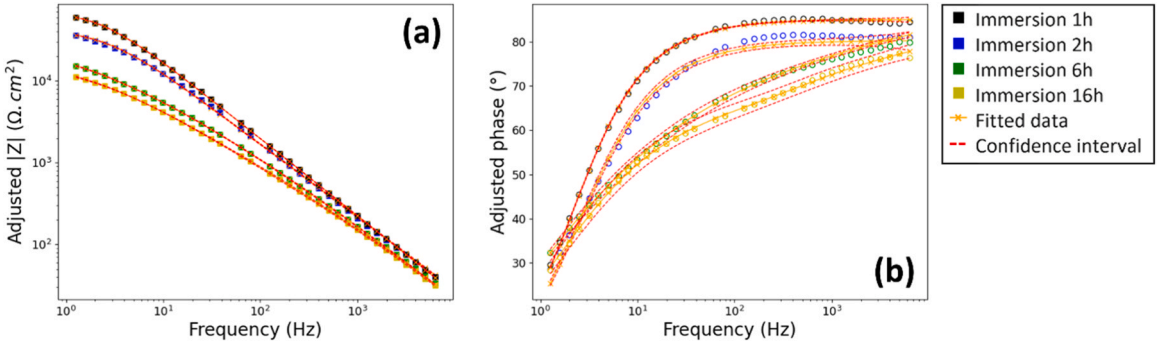

Fig. 7. Experimental adjusted and fitted Bode electrochemical impedance diagrams obtained at corrosion potential over immersion time: (a) impedance modulus and (b) phase angle as a function of frequency.

7×10^4 Ω.cm^2 to 10^4 Ω.cm^2 between 1 hour and 16 hours of immersion (Fig. 7.a). The phase angle as a function of frequency exhibits two distinct behaviors. At shorter times, the phase angle remains constant and is lower than −90° at high frequency. It is worth noting that the phase plateau decreases from −85° to −81° between 1 hour and 2 hours, respectively. For longer immersion time, the phase decreases monotonically with frequency, indicating a pseudo-CPE behavior.

The *ex-situ* SEM micrographs reveal an early-stage degradation of alumina layer on the hillocks grain boundary after 1 hour immersion (Fig. 8.a). Fig. 8.b illustrates the propagation of the degradation along the grain boundary. As immersion time progresses, the corrosion mode spreads toward the center of the copper grain, with the appearance of corrosion products (Fig. 8.c-d). The cross-sectional observations of localized corrosion after 16 hours of immersion reveal that the copper dissolution is limited to a depth of 200 nm. The tortuous morphology of the corrosion products and copper dissolution is clearly visible, with a complex geometry inside the corrosion defects. However, there is no apparent continuity of these corrosion products, creating a free pathway for the electrolyte to reach the underlying copper. It was verified that there was no corrosion after 16 hours immersion under the same conditions for a sample with no hillocks (Fig. 9a), on its surface, whereas the corrosion was observed for the covered copper for covered copper with hillocks (Fig. 9b). This indicates that it is indeed the thinning of ALD Al_2O_3 layer on the edges of the copper hillocks that leads to the corrosion sensitivity of the coated copper, in agreement with the modification of the electrochemical signature over the immersion time in the neutral, aerated and chlorinated solution.

The localized initiation and propagation of the coated-copper corrosion in neutral environment can be explained using a mechanism proposed by Diaz *et al.* [44]: when the irreversible oxygen reduction reaction takes place [45,46], hydroxide ions OH^- are formed close to the substrate in areas of confined porosity/discontinuity (Eq. 4), leading to brutal increase of the pH and alumina dissolution (Eq. 5):

$$O_2 + 2H_2O + 4e^- \rightarrow 4OH^- \quad (4)$$

$$Al_2O_3 + 2OH^- \rightleftarrows 2AlO_2^- + H_2O \quad (5)$$

In an environment containing chloride and at room temperature (~25°C), alumina has a relatively small pH stability range between about 4 and 9. Moreover, it is well known that the halogen anion penetrates at weak points of the oxide film to assist localized corrosion [47]. In the present case, these weak points are copper hillocks edge, where alumina layer is thinned. The anodic reaction is the copper oxidation. In the presence of complexing agents such as the chloride ions [Cl^-], Cu(I) reacts with the latter to form insoluble copper chloride CuCl (Eq. 6). Unstable, the corrosion products then react to form soluble complexes like $CuCl_2$ allowing Eq. 7, for example [45]:

$$Cu + Cl^- \rightleftarrows CuCl + e^- \quad (6)$$

$$CuCl + Cl^- \rightleftarrows CuCl_2^- \quad (7)$$

CuCl compounds react with water to form copper oxides by precipitation. The equilibrium of the reaction (Eq. 8) is shifted to the left when the concentration of chloride ion increases (decrease of the stability of Cu_2O) [44]:

$$2CuCl_2^- + 2OH^- \rightleftarrows Cu_2O + H_2O + 4Cl^- \quad (8)$$

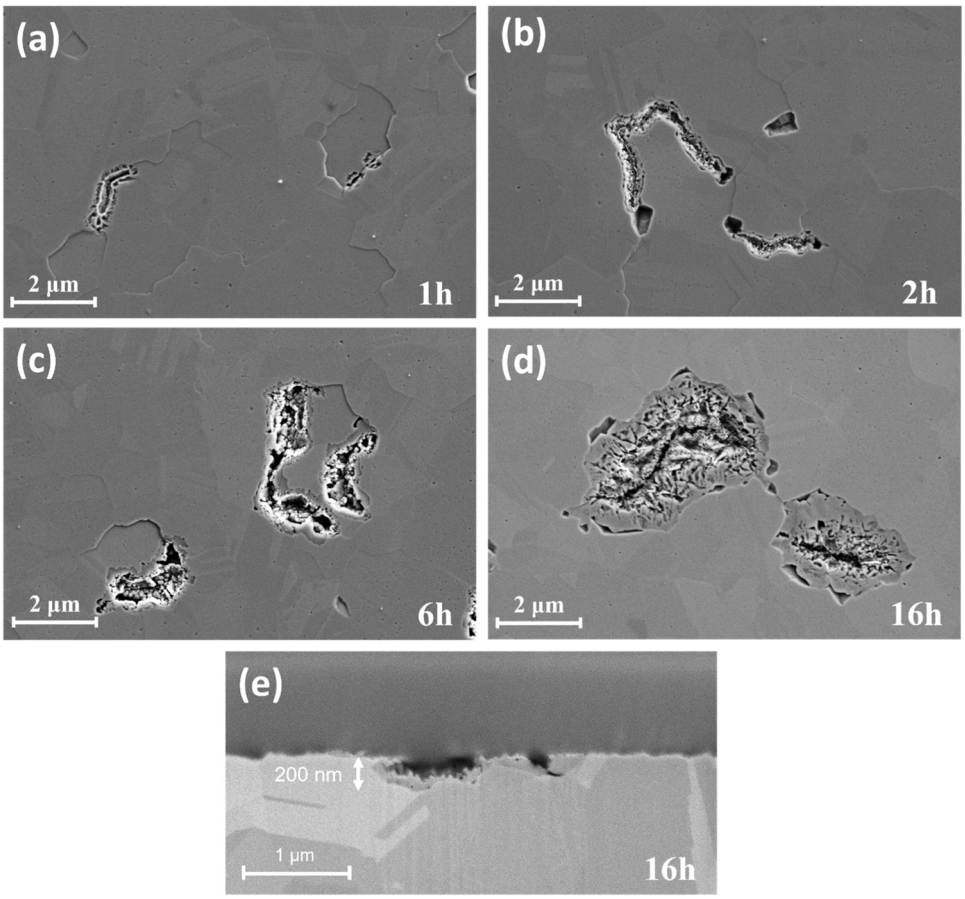

Fig. 8. SEM micrographs of 10 nm-thick alumina layer deposited on copper in 0.1 M NaCl solution after: (a) 1 hour, (b) 2 hours, (c) 6 hours and (d) 16 hours. (e) FIB cross-section of corrosion defect observed after 16 hours of immersion.

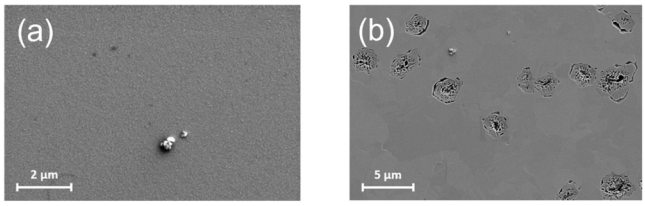

Fig. 9. SEM micrographs for the covered copper (a) a free of hillocks and (b) with hillocks after 16 hours of immersion in 0.1 M neutral chloride solution.

Based on these observations a further interpretation of experimental impedance diagrams can be proposed to build the models which allow to fit the data and to discuss the quantitative parameters evolutions.

For lower time, the slight phase shift reflects a non-ideal capacitive response of the alumina layer (Fig. 7). To account for this deviation from ideality, the constant phase element (CPE) was introduced [31,48]. Impedance of a CPE is defined by Eq. 9, according reference [48]:

$$Z_{CPE} = \frac{1}{Q_{CPE}(j\omega)^{\alpha}} \tag{9}$$

Where Q_{CPE} is a pseudo-capacitance with $\Omega^{-1}.cm^{-2}.s^{\alpha}$ units and α is a adimensional number between 0 and 1 reflecting non-ideality with respect to a pure capacitance (α = 1). The CPE parameters can be graphically extracted [36].

After 6 hours of immersion, the pure CPE behavior at high frequencies disappears in favor of a pseudo-CPE behavior attributed to Young impedance [49,50]. The Young impedance describes a decrease in resistivity from the metal/film interface to the film/electrolyte interface. This exponential distribution is expressed as shown in Eq. 10, and the calculation of the corresponding impedance Z(ω) is expressed allowing Eq. 11:

$$\rho(x) = \rho_0 \exp\left(\frac{-\delta}{\lambda}\right) \tag{10}$$

$$Z(\omega) = \frac{-\lambda}{j\omega\varepsilon\varepsilon_0} \ln\left[\frac{1 + j\omega\varepsilon\varepsilon_0\rho_0 \exp(-\delta/\lambda)}{1 + j\omega\varepsilon\varepsilon_0}\right] \tag{11}$$

Where ρ_0 is the resistivity at metal/film interface, δ is the thickness of the dielectric film, λ is the characteristic length of the decay.

To describe the two electrochemical behaviors observed during time, two electrical equivalent circuits are given in Fig. 10. For short immersion time, the model consists of a CPE in parallel with a resistance (Fig. 10.a). As immersion time increases, the model evolves to account for the reactivity of copper. A non-faradaic branch is composed of a double layer pseudo-capacitance (CPE_{dl}), while the faradaic branch consists of a Young's impedance in parallel with a resistance, consistent with result obtained in anodic domain (Fig. 6b). Since the Al_2O_3 layer is expected to be inert outside of the pitted region, the physical interpretation of the Young element is given by a mixed behavior between the Al_2O_3 layer and the discontinuous $CuCl/Cu_2O$ corrosion products at the bottom of the defects. The alumina layer electrochemical signature is expected to predominate over corrosion product with low insulating properties such as CuCl and Cu_2O. For example, CuCl compounds are known to have very low dielectric constants [51] (ε = 0.1), while Cu_2O corrosion products are reported to be porous [52]. As the impedance data were corrected by the electrolyte resistance, this parameter was not included in either model.

The fitted impedance diagrams are presented in Fig. 7 in straight

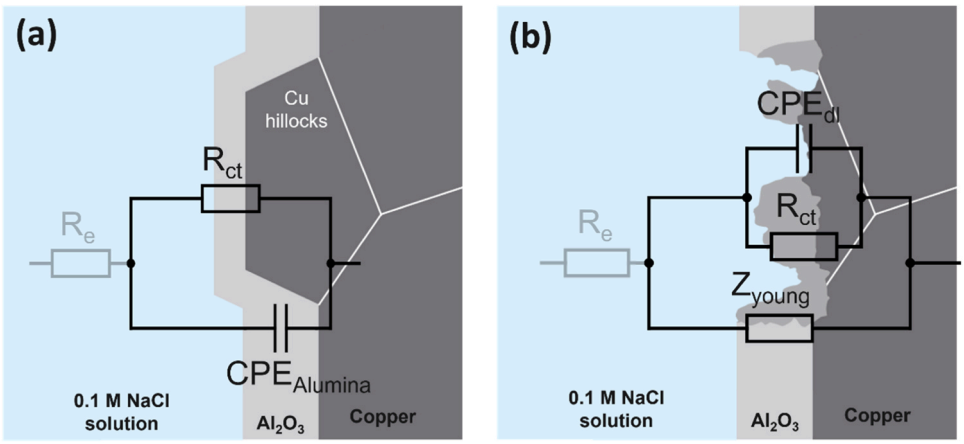

Fig. 10. Electrical equivalent circuits used to fit the impedance diagrams obtained: (a) at short time (< 6 h) and (b) longer time of immersion.

orange lines and show good correspondence with experimental diagrams. The red dashed lines represent the confidence intervals for the data (± 2σ). The phase values is more sensitive, resulting in broader confidence intervals (Fig. 7.b). Table 2 displays the fitted parameters obtained from using of model EEC (a) corresponding to impedance diagrams obtained after 1 hour and 2 hours. The values of the CPE parameter are consistent with the presence of an oxide layer [53]. The polarisation resistance is close to the fitted resistance. Thus, the fitted resistance can be attributed to the charge transfer resistance by comparison with the obtained resistance in sodium sulfate medium (Table 1). It should be noted the charge transfer resistance decrease by almost 50% during the first 2 hours of immersion.

The fitted parameters obtained for longer immersion time and using EEC (Fig. 10.b) are presented in Table 3. As previously discussed, the polarization resistance was assumed to be equal to the charge transfer resistance. Therefore, the R_{ct} value was fixed at the experimental R_p value to guide in the fitting process. The values of the CPE parameters correspond to typical values for a double layer capacitor ($\alpha \sim 0.7$ and $Q \sim 10^{-5}$ $\Omega.cm^{-2}.s^{\alpha}$) and remain constant over time. The polarization resistance decreases from 47.2 $k\Omega.cm^2$ to almost 29.7 $k\Omega.cm^2$ between 4 and 6 hours before stabilizing. The thickness obtained at the copper/alumina layer/NaCl electrolyte has been observed to increase, while the resistivity fitter has been observed to decrease over time. These results could be attributed to the modification of the dielectric layer parameters resulting from the formation of localized copper corrosion products and the thinning or dissolution of the alumina layer, in agreement with the SECM investigation (Fig. 5). This is consistent with the surface state observations depicted in Fig. 8c-e.

The link between the electrochemical behavior and the surface state observations has been established through the employed procedure. This has been done in order to gain a better understanding of the corrosion failure of microelectronic devices.

4. Conclusion

The present study employed a multidisciplinary approach that combined electrochemistry and surface analysis to investigate the corrosion issues of microelectronic copper pads covered with 10 nm-thick alumina layer deposited via ALD. Among the techniques employed, impedance spectroscopy emerged as a crucial tool. This versatile technique enables the characterization of thin layer materials, as well as the identification of degradation mechanisms, depending on the type of electrolyte used.

The durability of the coated system was shown to be relatively poor in 0.1 M NaCl medium, with a reduction in corrosion protection from the first hours. It was proposed that the alumina layer is weakened and thinned in the areas close to hillocks grain boundary due to internal mechanical constraints. This local thinning, combined with the aggressive action of halides, was responsible for the mechanism of corrosion on the whole hillocks grain. A local increase of pH was assumed, linked to the dissolved oxygen reduction in the areas where the copper is exposed. This phenomenon exacerbated the local dissolution of Al_2O_3, revealing the areas of high reactivity. The tortuous corrosion morphology observed was associated with preferential dissolution of the copper.

By gaining a better understanding of the degradation mechanism specific to these types of materials, it is now possible to propose material conceptualizations to fulfill industrial requirement.

Table 2
Fitted data obtained from EEC (a) (Fig. 9.a).

Time	α_{film}	Q_{film} $\mu\Omega^{-1}.cm^{-2}s^{\alpha}$	R_{ct} $k\Omega.cm^2$	χ^2	R_p* $k\Omega.cm^2$
1 h	0.94	1.15	71.6	3.05×10^{-3}	74.7
2 h	0.89	1.89	43.8	4.30×10^{-2}	49.0

* The polarization resistance R_p is obtained independently and added to validate the fitted values.

Table 3
Fitted data obtained from EEC, Fig. 10.b.

Time	α_{dl}	Q_{dl} $\mu\Omega^{-1}.cm^{-2}s^{\alpha}$	ρ_0 $\Omega.cm$	δ nm	λ nm	χ^2	R_p* $k\Omega.cm^2$
4 h	0.68	4.57	5.41×10^{12}	12.2	2.14	1.21×10^{-2}	47.2
6 h	0.66	8.17	1.07×10^{12}	12.3	2.75	1.04×10^{-3}	29.7
8 h	0.69	7.61	3.99×10^{11}	12.8	2.53	6.38×10^{-4}	23.2
10 h	0.70	7.34	3.14×10^{11}	12.9	2.19	1.04×10^{-3}	20.8
12 h	0.69	8.87	3.29×10^{11}	15.7	2.51	2.23×10^{-3}	21.1
14 h	0.69	1.17	6.31×10^{11}	15.8	2.36	7.52×10^{-3}	22.0
16 h	0.63	1.50	8.99×10^{11}	14.9	2.23	1.14×10^{-2}	22.2

* The polarization resistance R_{pol} is obtained independently and added to validate the fitting values.

Author Statement

On behalf of all the authors of this manuscript, I certify the following as appropriate:

- All authors have participated in (*i*) conception and design, or analysis and interpretation of the data (*ii*) drafting the article or revising it critically for important intellectual content; and (*iii*) approval of the final version.
- This manuscript has not been submitted to, nor is under review at, another journal or other publishing venue.

- The authors have no affiliation with any organization with a direct or indirect financial interest in the subject matter discussed in the manuscript.

CRediT authorship contribution statement

Lucile Broussous: Writing – review & editing, Supervision, Project administration, Funding acquisition. **Lucie Mazet:** Investigation, Formal analysis, Data curation. **Bernard Normand:** Writing – review & editing, Validation, Supervision, Project administration, Conceptualization. **Romain Haeffele:** Writing – original draft, Methodology, Investigation, Formal analysis, Data curation. **Sabrina Marcelin:** Writing – review & editing, Writing – original draft, Validation, Supervision, Methodology, Formal analysis.

Declaration of Competing Interest

The authors declare that they have no known competing financial interests or personal relationships that could have appeared to influence the work reported in this paper.

Data Availability

Data will be made available on request.

References

[1] R. Rongen, G.M. O'Halloran, A. Mavinkurve, L. Goumans, M.-L. Farrugia, Lifetime prediction of Cu-Al wire bonded contacts for different mould compounds, 2014 IEEE 64th Electron. Compon. Technol. Conf. (ECTC), Orlando, FL, USA (2014) 411–418, https://doi.org/10.1109/ECTC.2014.6897318.

[2] T. Boettcher, M. Rother, S. Liedtke, M. Ulrich, M. Bollmann, A. Pinkernelle, D. Gruber, H.-J. Funke, M. Kaiser, K. Lee, M. Li, K. Leung, T. Li, M.L. Farrugia, O. O'Halloran, M. Petzold, B. März, R. Klengel, On the intermetallic corrosion of Cu-Al wire bonds, 2010 12th Electron. Packag. Technol. Conf., Singap. (2010) 585–590, https://doi.org/10.1109/EPTC.2010.5702706.

[3] H. Abe, D.C. Kang, T. Yamamoto, T. Yagihashi, Y. Endo, H. Saito, T. Horie, H. Tamate, Y. Ejiri, N. Watanabe, T. Iwasaki, Cu wire and Pd-Cu wire package reliability and molding compounds, 2012 IEEE 62nd Electron. Compon. Technol. Conf. San. Diego, CA, USA (2012) 1117–1123, https://doi.org/10.1109/ECTC.2012.6248975.

[4] S.H. Kim, J.W. Park, S.J. Hong, J.T. Moon, The interface behavior of the Cu-Al bond system in high humidity conditions, 2010 12th Electron. Packag. Technol. Conf., Singap. (2010) 545–549, https://doi.org/10.1109/EPTC.2010.5702699.

[5] S. Murali, N. Srikanth, C. J. V III, Effect of wire size on the formation of intermetallics and Kirkendall voids on thermal aging of thermosonic wire bonds, Mater. Lett. 58 (2004) 3096–3101, https://doi.org/10.1016/j.matlet.2004.05.070.

[6] L.L. Jinzhi, C. Yan, W. Bisheng, L. Xiaomin, F. Chao, H. Younan, A review on the copper bond pad application in wire bond technique, 19th Int. Conf. Electron. Packag. Technol. (ICEPT), Shanghai, China (2018) 1546–1553, https://doi.org/10.1109/ICEPT.2018.8480485.

[7] R.P. Vinci, E.M. Zielinski, J.C. Bravman, Thermal strain and stress in copper thin films, Thin Solid Films 262 (1995) 142–153, https://doi.org/10.1016/0040-6090(95)05834-6.

[8] S.P. Murarka, I.V. Verner, R.J. Gutmann, Copper - Fundamental Mechanisms for Microelectronic Application, Wiley, 2000.

[9] H.-H. Strehblow, H.D. Speckmann, Corrosion and layer formation of passive copper in alkaline solutions, Mater. Corros. 35 (1984) 512–519, https://doi.org/10.1002/maco.19840351104.

[10] M. Honkanen, M. Vippola, T. Lepistö, Low temperature oxidation of copper alloys—AEM and AFM characterization, J. Mater. Sci. 42 (2007) 4684–4691, https://doi.org/10.1007/s10853-006-0351-x.

[11] M.-L. Chang, T.C. Cheng, M.C. Lin, H.-C. Lin, M.-F. Chen, Improvement of oxidation resistance of copper by atomic layer deposition, Appl. Surf. Sci. 258 (2012) 10128–10134, https://doi.org/10.1016/j.apsusc.2012.06.090.

[12] G.G. Harman, C.E. Johnson, Wire bonding to advanced copper, low-K integrated circuits, the metal/dielectric stacks, and materials considerations (Dec.), IEEE Trans. Compon. Packag. Technol. vol. 25 (4) (2002) 677–683, https://doi.org/10.1109/TCAPT.2002.808008.

[13] M.B. Tabiera, B.C.S. Bacquian, T.D. Lacuesta, Wirebond enhancement on copper palladium bonding in a over pad metalization, IEEE 16th Electron. Packag. Technol. Conf. (EPTC), Singap. (2014) 220–224, https://doi.org/10.1109/EPTC.2014.7028301.

[14] P. Ratchev, S. Stoukatch, B. Swinnen, Mechanical reliability of Au and Cu wire bonds to Al, Ni/Au and Ni/Pd/Au capped Cu bond pads, Microelectron. Reliab. 46 (2006) 1315–1325, https://doi.org/10.1016/j.microrel.2005.11.002.

[15] J.-N. Aoh, C.-L. Chuang, Thermosonic bonding of gold wire onto a copper pad with titanium thin-film deposition, J. Electron. Mater. 33 (2004) 290–299, https://doi.org/10.1007/s11664-004-0135-5.

[16] J. Chen, D. Degryse, P. Ratchev, I. De Wolf, Mechanical issues of Cu-to-Cu wire bonding, IEEE Trans. Compon. Packag. Technol. vol. 27 (3) (2004) 539–545 (Sept.).

[17] R. Haneda, K. Aramaki, Protection of copper corrosion by an ultrathin two-dimensional polymer film of alkanethiol monolayer, J. Electrochem. Soc. 145 (1998) 1856–1861, https://doi.org/10.1149/1.1838567.

[18] H.M. Ho, W. Lam, S. Stoukatch, P. Ratchev, C. J. V III, E. Beyne, Direct gold and copper wires bonding on copper, Microelectron. Reliab. 43 (2003) 913–923, https://doi.org/10.1016/S0026-2714(03)00074-X.

[19] R.W. Johnson, A. Hultquist, S.F. Bent, A brief review of atomic layer deposition: from fundamentals to applications, Mater. Today 17 (2014) 236–246, https://doi.org/10.1016/j.mattod.2014.04.026.

[20] M.J. Biercuk, D.J. Monsma, C.M. Marcus, J.S. Becker, R.G. Gordon, Low-temperature atomic-layer-deposition lift-off method for microelectronic and nanoelectronic applications, Appl. Phys. Lett. 83 (2003) 2405–2407, https://doi.org/10.1063/1.1612904.

[21] Y. Zhang, D. Seghete, A. Abdulagatov, Z. Gibbs, A. Cavanagh, R. Yang, S. George, Y.-C. Lee, Investigation of the defect density in ultra-thin Al_2O_3 films grown using atomic layer deposition, Surf. Coat. Technol. 205 (2011) 3334–3339, https://doi.org/10.1016/j.surfcoat.2010.12.001.

[22] G.C. Correa, B. Bao, N.C. Strandwitz, Chemical stability of titania and alumina thin films formed by atomic layer deposition, ACS Appl. Mater. Interfaces 7 (2015) 14816–14821.

[23] M.K. Tripp, C. Stampfer, D.C. Miller, T. Helbling, C.F. Herrmann, C. Hierold, K. Gall, S.M. George, V.M. Bright, The mechanical properties of atomic layer deposited alumina for use in micro- and nano-electromechanical systems, Sens. Actuator A Phys. 130 (2006) 419–429, https://doi.org/10.1016/j.sna.2006.01.029.

[24] J.S. Daubert, G.T. Hill, H.N. Gotsch, A.P. Gremaud, J.S. Ovental, P.S. William, C. J. Oldham, G.N. Parsons, Corrosion protection of copper using Al2O3, TiO2, ZnO, HfO2, and ZrO_2 atomic layer deposition, ACS Appl. Mater. Interfaces 9 (2017) 4192–4201, https://doi.org/10.1021/acsami.6b13571.

[25] Z. Chai, J. Li, X. Lu, D. He, Use of electrochemical measurements to investigate the porosity of ultra-thin Al_2O_3 films prepared by atomic layer deposition, RSC Adv. 4 (2014) 39365–39371, https://doi.org/10.1039/C4RA04565C.

[26] M.A. Fusco, C.J. Oldham, G.N. Parsons, Investigation of the corrosion behavior of atomic layer deposited Al_2O_3/TiO_2 nanolaminate thin films on copper in 0.1 M NaCl, Materials 12 (2019) 672–696, https://doi.org/10.3390/ma12040672.

[27] Z. Chai, Y. Liu, J. Li, X. Lu, D. He, Ultra-thin Al_2O_3 films grown by atomic layer deposition for corrosion protection of copper, RSC Adv. 4 (2014) 50503–50509, https://doi.org/10.1039/C4RA09179E.

[28] S. Mirhashemihaghighi, L.H. Klein, E. Harkonen, M. Ritala, P. Marcus, Electrochemical and surface analysis of the corrosion protection of copper by nanometer-thick alumina coatings prepared by atomic layer deposition, J. Electrochem. Soc. 162 (2015) C377–C384, https://doi.org/10.1149/2.0081508jes.

[29] A. van der Lee, Grazing incidence specular reflectivity: theory, experiment, and applications, Solid State Sci. 2 (2000) 257–278, https://doi.org/10.1016/S1293-2558(00)00119-9.

[30] W. Watson, M.E. Orazem, EIS: Measurement Model Program, ECSarXiv, Sep. 16, 2020. doi:10.1149/osf.io/kze9x.

[31] J.-B. Jorcin, M.E. Orazem, N. Pébère, B. Tribollet, CPE analysis by local electrochemical impedance spectroscopy, Electrochim. Acta 51 (2006) 1473–1479, https://doi.org/10.1016/j.electacta.2005.02.128.

[32] S. Marcelin, Z. Zhang, B. Ter-Ovanessian, B. Normand, Relationship between the resistivity profiles obtained from the power law model and the physico-chemical properties of passive films, J. Electrochem. Soc. 168 (2021) 021503–021511, https://doi.org/10.1149/1945-7111/abde84.

[33] A. Timma, P. Caubet, B. Chenevrier, O. Thomas, B. Kaouache, Post Si(C)N hillock nucleation and growth in IC copper lines controlled by diffusional creep, Microelectron. Eng. 87 (2010) 361–364, https://doi.org/10.1016/j.mee.2009.08.003.

[34] M.M. Nowell, D.P. Field, Texture and grain boundary structure dependence of hillock formation in thin metal films, MRS Online Proc. Libr. 516 (1998) 115–120, https://doi.org/10.1557/PROC-516-115.

[35] A. Basavalingappa, J.R. Lloyd, Effect of microstructure and anisotropy of copper on reliability in nanoscale interconnects, IEEE Trans. Device Mater. Reliab. 17 (2017) 69–79, https://doi.org/10.1109/TDMR.2017.2655459.

[36] M.E. Orazem, N. Pébère, B. Tribollet, Enhanced graphical representation of electrochemical impedance data, J. Electrochem. Soc. 153 (2006) B129–B136, https://doi.org/10.1149/1.2168377.

[37] M.E. Orazem, B. Tribollet, Electrochemical Impedance Spectroscopy, John Wiley & Sons, New Jersey, 2008.

[38] K.S. Cole, R.H. Cole, Dispersion and absorption in dielectrics I. Alternating current characteristics, J. Chem. Phys. 9 (1941) 341–351, https://doi.org/10.1063/1.1750906.

[39] M. Benoit, C. Bataillon, B. Gwinner, F. Miserque, M.E. Orazem, C.M. Sánchez-Sánchez, B. Tribollet, V. Vivier, Comparison of different methods for measuring the passive film thickness on metals, Electrochim. Acta 201 (2016) 340–347. ⟨https://doi.org/10.1016/j.electacta.2015.12.173⟩.

[40] F. Argall, A. Jonscher, Dielectric properties of thin films of aluminium oxide and silicon oxide, Thin Solid Films 2 (1968) 185–210, https://doi.org/10.1016/0040-6090(68)90002-3.

[41] M.D. Groner, J.W. Elam, F.H. Fabreguette, S.M. George, Electrical characterization of thin Al_2O_3 films grown by atomic layer deposition on silicon and various metal substrates, Thin Solid Films 413 (2002) 186–197, https://doi.org/10.1016/S0040-6090(02)00438-8.
[42] E. Warburg, Ueber das Verhalten sogenannter unpolarisirbarer Elektroden gegen Wechselstrom, Ann. Phys. 303 (1899) 493–499, https://doi.org/10.1002/andp.18993030302.
[43] H.S. Bahari, H. Savaloni, Surface analysis of Cu coated with ALD Al_2O_3 and its corrosion protection enhancement in NaCl solution: EIS and polarization, Mater. Res. Express 6 (2019) 086570–086585, https://doi.org/10.1088/2053-1591/ab1abd.
[44] B. Díaz, E. Härkönen, V. Maurice, J. Światowska, A. Seyeux, M. Ritala, P. Marcus, Failure mechanism of thin Al_2O_3 coatings grown by atomic layer deposition for corrosion protection of carbon steel, Electrochim. Acta 56 (2011) 9609–9618, https://doi.org/10.1016/j.electacta.2011.07.104.
[45] G. Kear, B.D. Barker, F.C. Walsh, Electrochemical corrosion of unalloyed copper in chloride media—a critical review, Corros. Sci. 46 (2004) 109–135, https://doi.org/10.1016/S0010-938X(02)00257-3.
[46] C. Deslouis, B. Tribollet, G. Mengoli, M.M. Musiani, Electrochemical behaviour of copper in neutral aerated chloride solution. I. Steady-state investigation, J. Appl. Electrochem. 18 (1988) 374–383, https://doi.org/10.1007/BF01093751.
[47] F. Dabosi, G. Beranger, B. Baroux, Corrosion localisée, les éditions de physique, 2012.
[48] G.J. Brug, A.L. van den Eeden, M. Sluyters-Rehbach, J.H. Sluyters, The analysis of electrode impedances complicated by the presence of a constant phase element, J. Electroanal. Chem. Interfacial Electrochem. 176 (1984) 275–295, https://doi.org/10.1016/S0022-0728(84)80324-1.
[49] L. Young, Anodic oxide films. Part 4.-The interpretation of impedance measurements on oxide coated electrodes on niobium, Trans. Faraday Soc. 51 (1995) 1250–1260, https://doi.org/10.1039/TF9555101250.
[50] C.A. Schiller, W. Strunz, The evaluation of experimental dielectric data of barrier coatings by means of different models, Electrochim. Acta 46 (2001) 3619–3625, https://doi.org/10.1016/S0013-4686(01)00644-2.
[51] C. You, S. Briggs, M.E. Orazem, Model development methodology for localized corrosion of copper, Corros. Sci. 222 (2023) 111388–112402, https://doi.org/10.1016/j.corsci.2023.111388.
[52] B. Ibrahim, D. Zagidulin, M. Behazin, S. Ramamurthy, J. Wren, D. Shoesmith, The corrosion of copper in irradiated and unirradiated humid air, Corros. Sci. 141 (2018) 53–62, https://doi.org/10.1016/j.corsci.2018.05.024.
[53] M.E. Orazem, I. Frateur, B. Tribollet, V. Vivier, S. Marcelin, N. Pébère, A.L. Bunge, E.A. White, D.P. Riemer, M. Musiani, Dielectric properties of materials showing constant-phase-element (CPE) impedance response, J. Electrochem. Soc. 160 (2013) C215–C225, https://doi.org/10.1149/2.033306jes.